Characteristics of VIRS Signals within Pixels of TRMM PR for Warm Rain in the Tropics and Subtropics

YILUN CHEN

School of Earth and Space Sciences, University of Science and Technology of China, Hefei, China

YUNFEI FU

School of Earth and Space Sciences, University of Science and Technology of China, Hefei, and State Key Laboratory of Severe Weather, Chinese Academy of Meteorological Sciences, Beijing, China

(Manuscript received 3 June 2016, in final form 28 November 2016)

ABSTRACT

Many data-merging studies of the Tropical Rainfall Measuring Mission (TRMM) satellite involve the integration of high-resolution Visible and Infrared Scanner (VIRS) signals (~2 km) with low-resolution Precipitation Radar (PR) footprint (~5 km) to obtain comprehensive information from observations. Based on the merged dataset, ''warm rain'' is generally identified as having averaging 10.8-μm brightness temperatures ($TB_{10.8}$) exceeding 273 K and the existence of surface rainfall. However, this integration may lead to the misidentification of warm rain because the beam-filling problem (nonuniform $TB_{10.8}$ in PR pixels) is not fully considered through the method using high-resolution $TB_{10.8}$ to match low-resolution rainfall. To assess the bias that is associated with identifying warm rain, a new dataset that includes all VIRS signals within the PR resolution is established, and the characteristics of this warm rain in the summers of 1998–2012 are analyzed. The results show that clear-sky pixels and ''cold'' pixels probably exist in some apparent warm-rain cases (60.5% and 11.2% of the time, respectively). According to this finding, warm-rain pixels are divided into pixels with and without clear sky. Statistical analysis shows that the existence of clear-sky pixels has a huge influence on the characteristics of the warm-rain pixels. The implications of this study are that many of the warm-rain cases are in fact not warm rain. When studying warm rain, the situation whereby the edges of pixels are clear sky should be fully considered. Also, when computing the weighted average brightness temperature and other characteristics of warm-rain pixels, parts that are clear-sky or cold pixels should be expelled to mitigate beam-filling problems.

1. Introduction

''Warm cloud'' refers to cloud whose temperature at the cloud top is higher than 0°C (273 K or 32°F), thus consisting only of liquid water drops. And the rainfall produced by such cloud is referred to as ''warm rain'' (Beard and Ochs 1993). Warm rain is an important part of precipitation systems in the tropics and subtropics. Sometimes, it is accompanied by deep convective precipitation (Schumacher and Houze 2003). On account of observational experiments like the Warm Rain Project (Lavoie 1967), the Barbados Oceanographic and Meteorological Experiment (Holland and Rasmusso 1973), and the First International Satellite Cloud Climatology Project (ISCCP) Regional Experiment (Cox et al. 1987), experts began to systematically study the microphysical features and radiation characteristics of warm cloud (including trade wind cumulus and marine stratocumulus; Beard and Ochs 1993; Lau and Wu 2003; Kubar et al. 2009; Min et al. 2013). For instance, Lau and Wu (2003) suggested that tropical warm rain covers 72% of the full precipitation area. And Min et al. (2013) developed a set of physical algorithms to retrieve the latent heat of warm rain on the basis of its dynamic and thermodynamic characteristics.

Because warm rain mostly occurs over the oceans in the tropics and subtropics, conventional observational methods (such as ground pluviometers) are barely applicable because of their low distributing density in such areas. Instead, the use of satellite remote sensing technology to detect warm rain has emerged as offering distinct advantages. Since the 1980s, studies on warm rain have accomplished a considerable amount through the use of spectrum and microwave detectors loaded on

Corresponding author e-mail: Yunfei Fu, fyf@ustc.edu.cn

DOI: 10.1175/JAMC-D-16-0198.1

satellite platforms (Liu et al. 1995; Liu and Zipser 2009; Lebsock and L'Ecuyer 2011). Liu et al. (1995), for instance, used the results of microwave and infrared detection to reveal that about 14% of the raining area over the western Pacific Ocean could be classified as warm rain but that it only contributed around 4% to the total precipitation.

The Tropical Rainfall Measuring Mission (TRMM) was launched in November 1997 and equipped with the Visible and Infrared Sensor (VIRS) and Precipitation Radar (PR), which could actualize a synergetic observation to both spectral signals and precipitation (Fu et al. 2007; Liu et al. 2008; Liu et al. 2014; Yang et al. 2015). This offered an excellent opportunity to study warm rain. At present, VIRS pixels are usually merged onto PR pixels to identify warm rain, and this is achieved by using a thermal infrared brightness temperature threshold value of VIRS to identify warm cloud, with the PR to detect the precipitation features. Examples of studies that have used these data include Fu et al. (2007), who analyzed Typhoon Ranan over eastern China in 2004. They suggested that the proportion of warm rain in the typhoon's precipitation was 10%, and yet the proportion of warm cloud in nonprecipitation cloud was as high as 46%. Liu et al. (2008) established a rain-case database that was based on 9 yr of TRMM data and also included observations from VIRS and the TRMM Microwave Imager (TMI) merged onto each PR pixel. Subsequently, Liu and Zipser (2009) obtained the seasonal and spatial distribution of warm-rain cases based on this database.

Precipitation is highly asymmetric in spatial terms, and so the partial-filling effect may exist in the interior of pixels. This phenomenon has a noticeable effect on the observation and identification of warm rain. Previous studies on the precipitation partial-filling effect either compared echo signals from PR and ground or airborne radar (Gabella et al. 2011; Kirstetter et al. 2015) or compared the microwave-retrieved rain rate obtained from PR (Chiu and Petty 2006; Wilheit and Kummerow 2009; Liu and Zipser 2014). Many TRMM PR merged databases use the method of aggregating the VIRS brightness temperatures to the PR footprint (Liu et al. 2008; Liu and Fu 2010) but without consideration of the partial-filling effect of the VIRS pixels in the PR precipitation pixels (especially warm rain). There is usually a high temperature (273–290 K) at the cloud top in warm rain, but those pixels can be surrounded by mixed-cloud pixels (233–273 K) or clear-sky pixels. If the weighted average (Liu and Fu 2010) or nearest (Liu et al. 2008) thermal infrared brightness temperature is used to identify warm cloud, these surrounding mixed-cloud pixels or clear-sky pixels may be judged as warm clouds. This problem can influence results on the properties of warm rain and its distribution.

To address these disadvantages, a new combined dataset of PR and VIRS over a 15-yr period (1998–2012) is established in the present study based on the merged dataset of TRMM PR and VIRS (Liu and Fu 2010). Warm-rain pixels during summer (June–August) over the tropical and subtropical (40°N–40°S) oceans are identified in the dataset. The intrinsic characteristics of pixels are studied, with the aim to expose the precipitation features and characteristics of warm rain in situations when they are filled by different kinds of VIRS pixels. It is expected that the present work will contribute to further research on the partial-filling effect of warm rain and help to improve methods for merging data from multiple instruments.

Following this introduction, section 2 introduces the data and methods used in the study. Samples and statistics were used to analyze the spectral characteristics and physical parameters in warm-rain pixels and the partial-filling effect that may exist, and these results are reported in section 3. A summary and conclusions are provided in section 4.

2. Data and method

The version-7 PR 2A25 data, produced by National Aeronautics and Space Administration Goddard Space Flight Center, were used in this study. This dataset provides rain type and 3D rain rate. The spatial distribution of the rain rate from mean sea level to 20 km is given by 2A25, whose vertical resolution is 250 m and horizontal resolution is 4.3 km. There are 49 pixels in each scanning line (Kummerow et al. 1998). The TRMM PR algorithm also classifies the rain type into convective, stratiform, and "other" (Steiner et al. 1995; Awaka et al. 1997). The 1B01 data include reflectivity (0.63 and 1.6 μm) and infrared radiation brightness temperature (3.7, 10.8, and 12 μm), which are calibrated from VIRS detected signals. The scanning swath of VIRS on Earth's surface is 720 km. There are 261 pixels on every scanning line, with a spatial resolution of 2.11 km at nadir (Kummerow et al. 1998). Despite the difference in spatial resolution between 2A25 and 1B01, the time difference between detection of one common target is less than 1 min. So, PR and VIRS can be considered as approximately synchronous in their detection.

To obtain the subpixel characteristics of warm rain, this section introduces the methods in three steps: First, the observations from 2A25 and 1B01 are spatially merged to establish a merged dataset. Then, a general method is used to identify warm rain. Using the merged dataset, subpixel characteristics are generated.

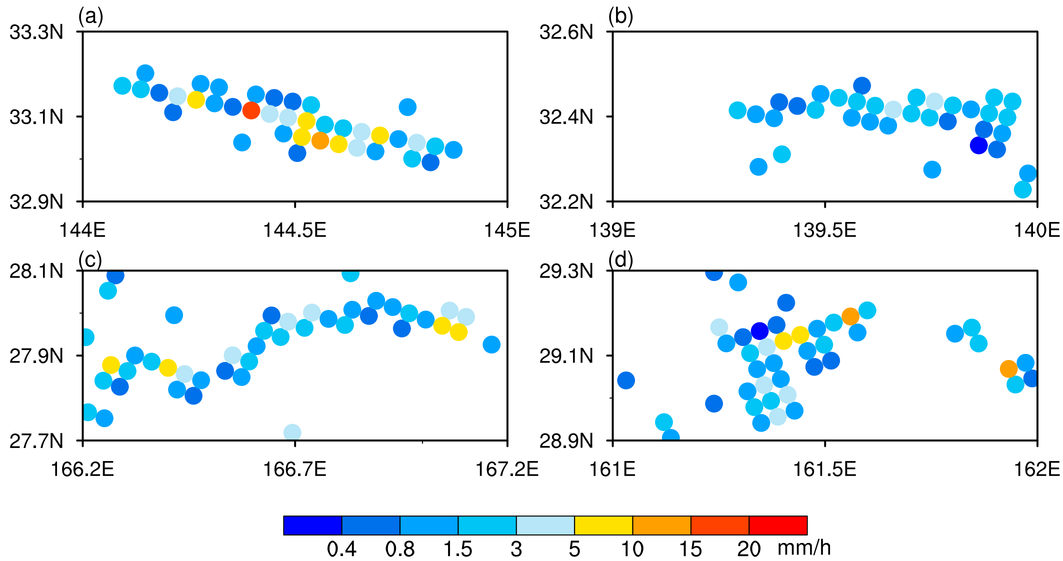

FIG. 1. Distribution of the near-surface rain rate of apparent warm-rain cases identified by the new dataset: orbits (a) 03874, (b) 03828, (c) 03704, and (d) 03701.

a. *Establishment of merged dataset*

In consideration of the fact that 2A25 is a 3D data product that can effectively identify precipitation, when 2A25 and 1B01 data are being merged, 1B01 signals are usually thrown onto 2A25 pixels rather than throwing 2A25 onto 1B01 (Liu et al. 2008; Liu and Fu 2010). Specifically, Liu et al. (2008) calculated the brightness temperature at each PR pixel from the nearest VIRS pixel; instead, Liu and Fu (2010) established a merged dataset at PR spatial resolution through a weighted average method. In this study, not only the weighted average infrared brightness temperature obtained from the merged data but also all the VIRS signals in the PR resolution are used to study the spectral characteristics in the interior of warm-rain pixels. Then, a new merged dataset is established.

b. *Identification of warm rain*

The thermal infrared channel of 10.8 μm ($TB_{10.8}$) is frequently used to identify the cloud phase near the cloud top. And warm rain is estimated via the 273-K brightness temperature threshold (Short and Nakamura 2000; Chen et al. 2011). Warm rain is identified if the weighted average $TB_{10.8}$ of precipitation pixels is higher than 273 K, and precipitation exists at the surface, which guarantees the reliability of warm-rain samples.

c. *Cloud classification in sub-PR pixel*

Monthly average sea surface temperature (SST), provided by the National Oceanic and Atmospheric Administration, is also used in this study. Plus, the multichannel SST (MCSST) algorithm, which was developed on the basis of VIRS, proposed by Guan et al. (2003), is used to retrieve the SST corresponding to VIRS pixels in every warm-rain pixel. The error of this retrieval method is less than 0.6 K. In view of the fact that ocean temperature retrieved from cloud pixels tends to be far lower than the actual ocean temperature, if the difference between the SST retrieved and the SST of reanalyzed data is less than 3 K, the area is recognized as clear sky. Considering the diurnal variation of SST and the error of the SST retrieval, 3 K is considered to be an appropriate threshold; besides, a 3-K threshold was also used by Liu et al. (1995) to categorize pixels as clear sky or cloud. This method is more suitable for both cold-ocean surfaces in the Southern Hemisphere and warm-ocean surfaces in the Northern Hemisphere, as compared with window brightness temperature.

For the convenience of producing figures to analyze the results at large scales, the coordinates of the PR pixels are interpolated to a 1° latitude–longitude grid.

3. Results

a. *Sample analysis*

The near-surface rain rate of four ‘‘apparent’’ warm-rain cases in the northwest Pacific Ocean is shown in Fig. 1, which means that each pixel in the four rain cases is a warm-rain pixel (weighted average $TB_{10.8}$ higher than 273 K). Precipitation features in the interior of warm-rain cases are exhibited by the four single samples, and they are not located at the edges of the PR

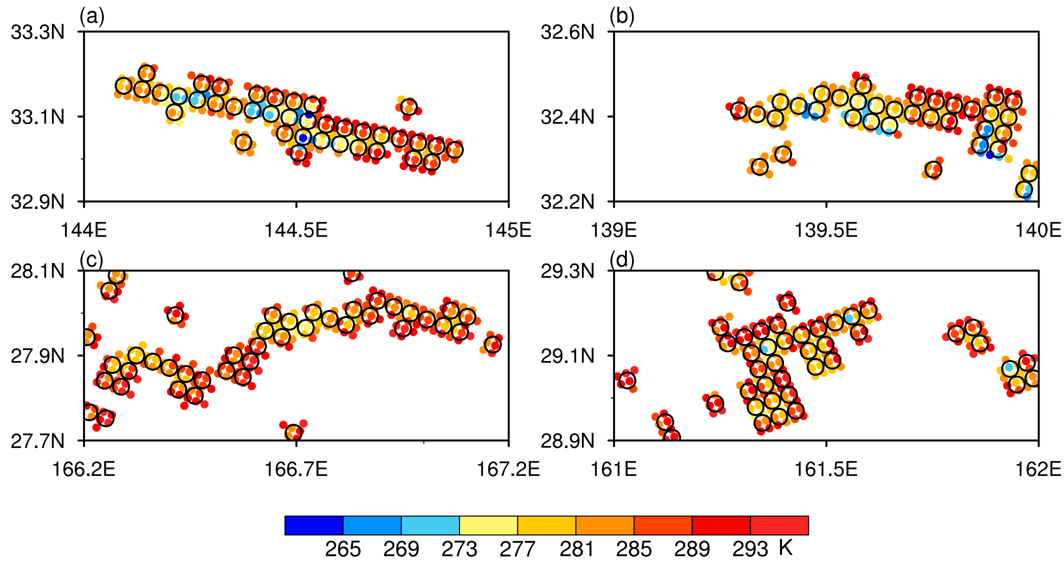

FIG. 2. As in Fig. 1, but for $TB_{10.8}$.

swaths. The scales of these four samples are all 30–100 km, namely, β mesoscale rain cases (Waymire et al. 1984). It can be seen that the rain cases depicted in Figs. 1a and 1c are longer and thinner, while that in Fig. 1d is squarer. Moreover, the discontinuity of the rain rate between two adjacent pixels is particularly apparent, in which the maximum difference could be greater than 10 mm h^{-1}. Pixels with a lower rain rate are usually located at the edges of rain cases.

The $TB_{10.8}$ of the above-mentioned four apparent warm-rain cases is shown in Fig. 2. The brightness temperature of this channel can be approximately taken as the cloud-top temperature. A color-scale change from blue to yellow is important, as it indicates the two sides of the critical temperature of 273 K. In Fig. 2a, the cloud-top temperature of two VIRS pixels is lower than 265 K, in the center of the rain case (at the position of approximately 144.5°E), which separately belong to two different PR pixels, and yet the $TB_{10.8}$ of other VIRS pixels is higher than 273 K. This makes the weighted average $TB_{10.8}$ of pixels higher than 273 K, meaning the pixels are recognized as warm-rain pixels. Information on merged pixels that are lower than 265 K will be arbitrarily expelled if brightness temperature is used to identify warm rain, which will cause a loss of intrinsic information. Likewise, if the nearest $TB_{10.8}$ is used to identify warm rain, loss of information may be more serious. All of the VIRS pixels' $TB_{10.8}$ values are higher than 273 K in Fig. 2c, but pixels higher than 293 K arise at the edges of rain cases. These pixels may actually be clear sky. If they are averaged to calculate the weighted average $TB_{10.8}$ in PR pixels, the cloud-top temperature will be overestimated.

In accordance with the method suggested in section 2, the difference in the monthly average SST of reanalyzed data and the SST retrieved by VIRS under a ''no cloud'' assumption is shown in Fig. 3. The 3-K threshold divides the VIRS pixels into clear pixels and cloudy pixels. There is not a big difference in the SST in the four areas in terms of monthly average; the range is 299–301 K. Since the difference between the VIRS-retrieved SST and background SST is used to discriminate cloudy from clear pixels, the critical values are highlighted by using the color scale from red to blue. In the center of apparent warm-rain cases, most of the VIRS pixels show color scale from yellow to blue, which suggests that there was actually cloud in the area. Likewise, at the southwestern side of Fig. 3a and the middle of Fig. 3b, some areas with cloud still exist although precipitation was not detected. But on the edge of many raining pixels, especially in rain cases in Figs. 3c and 3d, pixels where the retrieved SST is very close to the reanalyzed data suggest they are most likely clear-sky pixels. That is, inside that PR pixel, it is likely partially filled with cloud.

According to the approaches used to judge whether a clear-sky pixel exists, the weighted average $TB_{10.8}$ and maximum difference of the $TB_{10.8}$ of pixels with and without clear sky in the warm-rain cases mentioned above are shown in Fig. 4. ''Maximum difference'' of each warm-rain pixel is calculated by maximum $TB_{10.8}$ minus minimum $TB_{10.8}$ of VIRS pixels within the PR resolution. This parameter represents the variability of cloud top in the warm-rain pixel. For warm-rain pixels without clear sky, the weighted average $TB_{10.8}$ is pervasively 273–287 K, and the maximum difference of

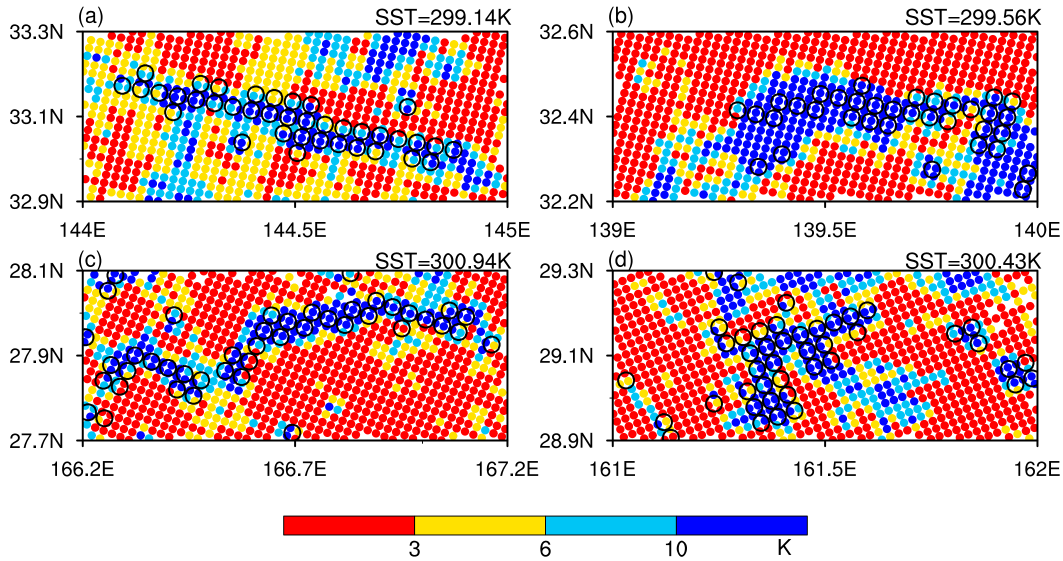

FIG. 3. As in Fig. 1, but for the difference in monthly average SST and the retrieved SST.

brightness temperature is 0–25 K. The maximum difference of $TB_{10.8}$ is narrowed as the weighted average $TB_{10.8}$ increases. When the weighted average $TB_{10.8}$ is 285 K, the maximum difference of brightness temperature can be as high as 15 K. There is a big difference between warm-rain pixels with clear sky and those without. The weighted average $TB_{10.8}$ of pixels with clear sky is mostly higher; however, the minimum should be 280 K, and pixels with a weighted average $TB_{10.8}$ higher than 290 K all belong to pixels with clear sky. When the weighted average $TB_{10.8}$ is constant, the maximum difference in $TB_{10.8}$ of pixels with clear sky is around 5 K higher than in pixels without clear sky.

b. *Statistical analysis*

It is necessary to determine the integral distributions of VIRS pixels in warm-rain pixels before distinguishing whether or not there is a pixel containing clear sky and then carrying out statistical analysis. The probability density functions (PDFs) of 0.63-μm reflectance ($RF_{0.63}$) and $TB_{10.8}$ during daytime [0800–1600 local time (LT)] and nighttime (2000–0400 LT) are separately shown in Fig. 5, in which there is no detected value of $RF_{0.63}$ at night. A double peak distribution is shown by $RF_{0.63}$; one peak value is about 0.15 and the other is 0.55. Generally, the $RF_{0.63}$ of the ocean surface is about 0.1, whereas a cloud pixel's $RF_{0.63}$ is mainly higher than 0.3. Thus, the peak value of 0.15 was very probably produced by clear-sky pixels. The proportion of $RF_{0.63}$ between 0 and 0.2 is about 20%, and thus it seems that the partial-filling effect generally exists in the warm-rain pixels. The daytime and nighttime $TB_{10.8}$ distributions resemble one another, both presenting a 282-K single-peak distribution, which suggests $TB_{10.8}$ was mildly influenced by time. Importantly, the $TB_{10.8}$ of part of the VIRS pixels is lower than 273 K, a proportion of 8% in all. If the weighted average $TB_{10.8}$ is used to judge warm cloud, the portion of these "cold" pixels will be taken as warm cloud. Similarly, at around 291–293 K in Fig. 5, the PDF does not reduce significantly, which may be the corresponding brightness temperature of clear-sky pixels. Although SST varies considerably in space and time, it changes far less than cloud-top

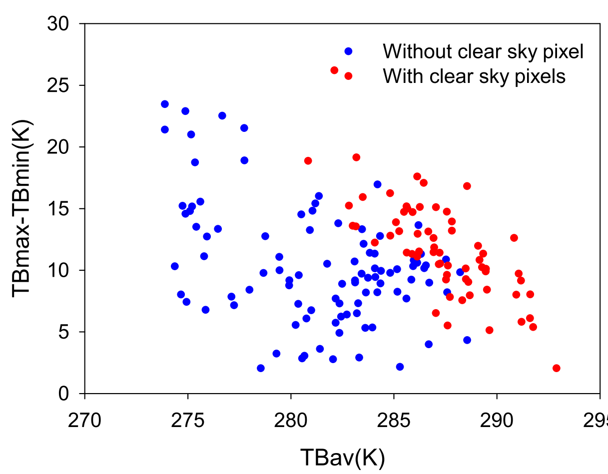

FIG. 4. Every pixel's weighted average $TB_{10.8}$ and maximum difference of $TB_{10.8}$ in the apparent warm-rain cases mentioned above (blue: pixels with clear sky; red: pixels without clear sky).

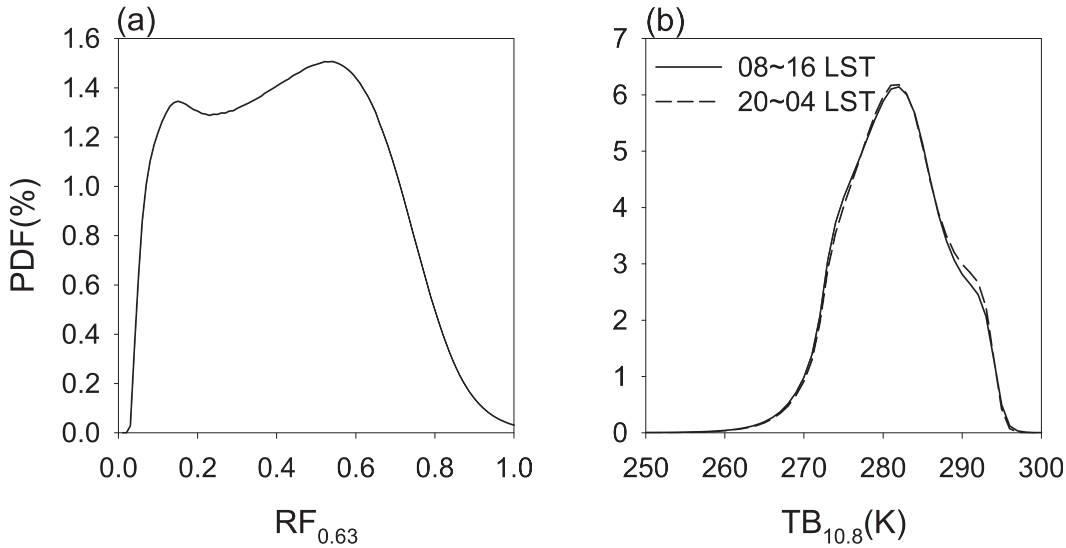

FIG. 5. PDFs of VIRS data in warm-rain pixels in summer 1998–2012 (solid lines stand for 0800–1600 LT; dashed line stands for 2000–0400 LT): (a) 0.63-μm reflectance and (b) $TB_{10.8}$.

temperature, so the pace of the PDF decline slows down in the SST window of $TB_{10.8}$.

To obtain the probability that partial-filling effect exists, Fig. 6 shows the probability of cold and clear-sky pixels within warm-rain pixels at 0800–1600 LT. It seems that the existence of cold pixels strongly correlates with the TB_{av}. The probability of cold pixels within warm-rain pixels decreases sharply from 70% (273 K) to lower than 10% (280 K). Yet there is a weak correlation between the RF_{av} and cold pixel probability. The probability of clear-sky pixels within warm-rain pixels shows a different distribution from cold pixel probability. Warm-rain pixels are more likely to contain clear-sky pixels with high TB_{av} and low RF_{av}, which is consistent with the spectral characteristics of clear sky. When the RF_{av} is higher than 0.4 and the TB_{av} is lower than 280 K, there is the minimum partial-filling effect caused by edge clear-sky pixels. Statistics show that

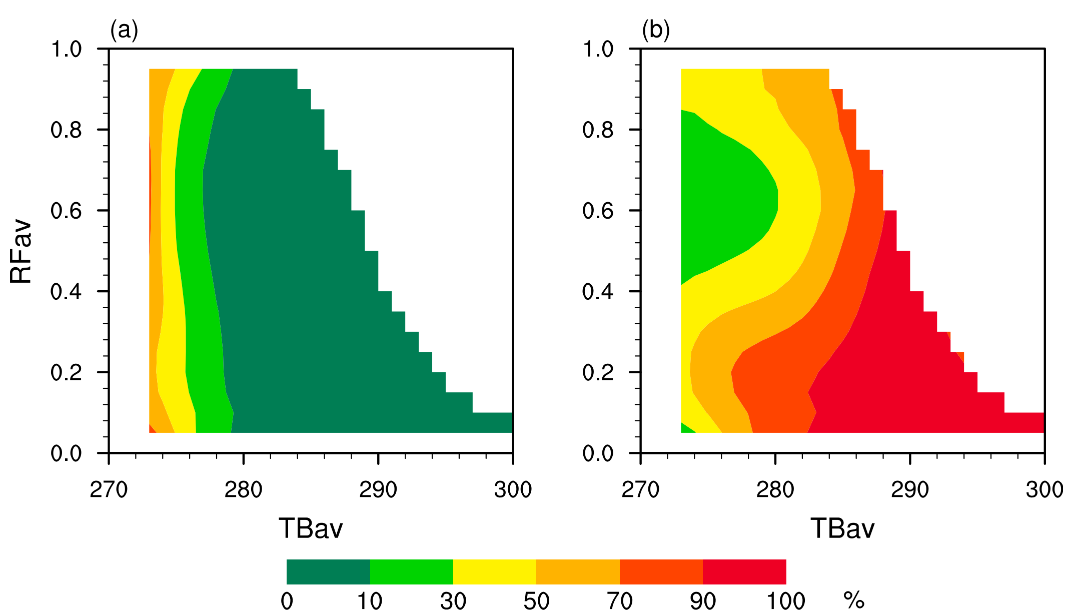

FIG. 6. The probability of (a) one or more VIRS pixel(s) lower than 273 K and (b) one or more clear-sky pixel (s) within warm-rain pixels at 0800–1600 LT.

clear-sky pixels are more common within warm-rain pixels than cold pixels. About 60.5% (11.2%) of the warm-rain pixels contain clear-sky (cold) pixels. That is, the partial-filling effect of clear-sky pixels is more serious than the partial-filling effect of cold pixels within warm-rain pixels.

For studying the general influence on warm-rain pixels by including clear-sky pixels, the spectral characteristics, 17-dBZ echo-top height, and rain rate (determined by whether there were clear-sky pixels in the summers of 1998–2012) are shown in Fig. 7. Resembling the sample results above, the weighted average $TB_{10.8}$ of warm-rain pixels without clear sky are mainly scattered under 287 K and the maximum difference of $TB_{10.8}$ changes very mildly—mainly lower than 10 K. However, the weighted average $TB_{10.8}$ of pixels with clear sky is mostly higher, and the difference in brightness temperature is also very large. The weighted average $TB_{10.8}$ is mostly distributed in the range 280–293 K and the difference in brightness temperature within 5–15 K, which is more concentrated than without clear-sky pixels in Fig. 7. Figures 7c and 7d show that, regardless of whether or not there is a clear-sky pixel in the warm-rain pixel, if the weighted average $TB_{10.8}$ is constant, the echo-top height will increase as the maximum difference of brightness temperature increases. The greater the maximum difference, the lower its minimum $TB_{10.8}$ and the higher the cloud top. That is, the pixels with a higher cloud top are able to lift up to the 17-dBZ echo-top height of the whole rain pixel. When the weighted average $TB_{10.8}$ is 285 K, the difference in brightness temperature is 5 K, and pixels with and without clear sky are both distributed here. At this time, the echo-top height of pixels with clear sky is 2.75 km, which is mildly higher than that of pixels without clear sky (2.25 km). As compared with the echo-top height, whether there is clear sky in a pixel has a clear impact on the rain rate. For warm-rain pixels without clear sky, their rain rate is mainly distributed within 1.6–3.2 mm h^{-1}, and yet the rain rate of that with clear sky is distributed in the range 1.2–2.4 mm h^{-1}, which is apparently lower than the rain rate of pixels without clear sky. When the weighted average $TB_{10.8}$ and maximum difference of $TB_{10.8}$ are given, the rain rate of warm rain with clear sky is around 0.4–0.8 mm h^{-1} lower than the rain rate of that without clear sky.

The visible channels of VIRS only detect values during daytime. So, for studying the influence of clear-sky pixels on warm-rain pixels' properties, samples during 0800–1600 LT were used. Prior to statistically analyzing each property, it is necessary to determine the spatial distribution of warm-rain samples, without clear sky, obtained from the above judging conditions (Fig. 8). Figure 8b shows the proportion of warm-rain samples without clear-sky pixels in all warm-rain samples. The results suggest that, in the majority of areas of the tropical and subtropical oceans (except near land), sample numbers without clear sky, in 1° grids, are all more than 10^2. Results have statistical significance based upon the sample numbers. Much warm rain exists in the mideast of the Pacific intertropical convergence zone (ITCZ). The numbers in grids can be as large as 500 over the Pacific ITCZ, and the proportion is around 40%–70%. There are also many warm-rain pixels on the two sides of the ITCZ from the middle to the western part of the Pacific Ocean, which is actually the warm tongue of SST. What is different is that there is less warm rain without clear sky in the northwestern part of the Pacific Ocean. There are only 100–300 samples in one grid, occupying a proportion of less than 30% in all warm-rain samples, whereas samples of warm rain without clear sky in grids in the southwestern part of the Pacific Ocean can be as many as 800 and yet occupy a proportion of more than 50% in all warm-rain samples. A situation in which warm rain without clear sky increases from north to south arises in the Indian Ocean. In the monsoon region, strong convective activity produces cold cores with warm-rain pixels mainly distributed at the edges of rain cases, and partial filling may arise more easily. Whereas temperature in the Southern Hemisphere is low, convection is weak, and central pixels in the rain case are also warm-rain pixels full of cloud. The spectral characteristics and echo-top height and rain rate of warm-rain pixels with and without clear sky are analyzed next.

$RF_{0.63}$ is sensitive to cloud and the ocean surface. Usually, the reflectance value of the ocean surface is less than that of cloud. The influence on the corresponding $RF_{0.63}$ of warm rain by whether a pixel has clear sky is exhibited in Figs. 9a and 9b. Overall, the $RF_{0.63}$ of warm rain pixels without clear sky is generally greater (mainly greater than 0.4), whereas the value of warm-rain pixels with clear sky is 0.2–0.5. In the northwest of the Pacific Ocean, the $RF_{0.63}$ of warm-rain pixels without clear sky is around 0.4–0.5, yet the $RF_{0.63}$ of that with clear sky is 0.2–0.3, which is about 0.2 smaller. In the Pacific ITCZ and areas around it and the Indian Ocean, the difference in $RF_{0.63}$ can be greater than 0.1. When compared with Fig. 2, what can be seen is at the resolution of a single rain pixel, generally 5–8 VIRS pixels can be matched. Once one of them is clear sky, its $RF_{0.63}$ is about 0.1, and the rest of the pixels are normal warm-rain pixels whose $RF_{0.63}$ values are around 0.5. If calculated through direct averaging, the last $RF_{0.63}$ will indeed be less than that of normal warm-rain pixels by about 0.1.

Thermal radiation information at the cloud top or clear sky at the land surface (ocean surface) is given by the $TB_{10.8}$ channel of VIRS, which is closely related to

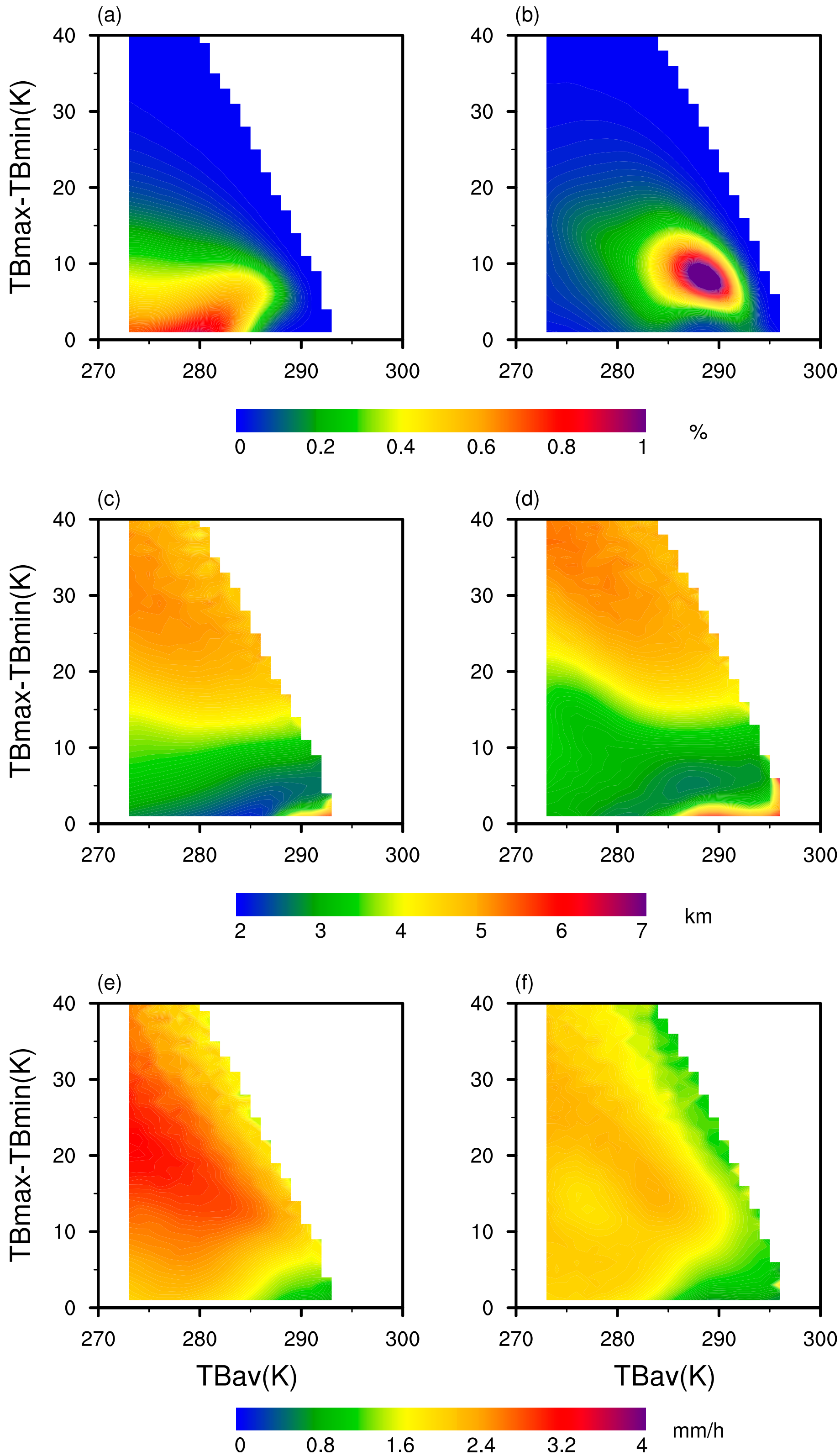

FIG. 7. Weighted average $TB_{10.8}$ and maximum difference of brightness temperature in warm-rain pixels (left) without clear sky and (right) with clear sky and their corresponding (a),(b) distribution, (c),(d) 17-dBZ echo-top height, and (e),(f) rain rate in summer 1998–2012.

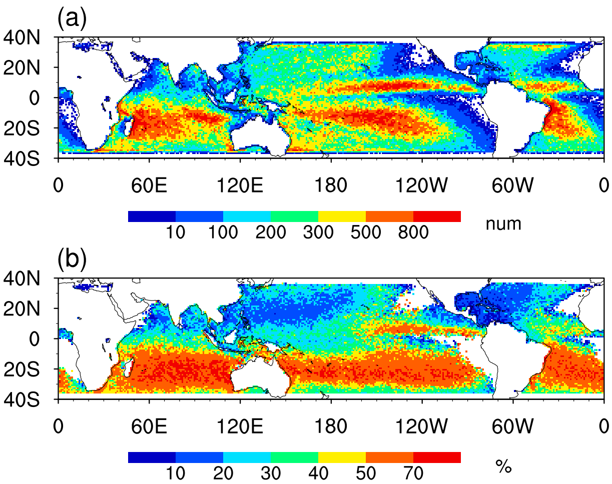

FIG. 8. Distributions during 0800–1600 LT in warm-rain pixels without clear sky: (a) total sample and (b) proportion.

the temperature of the cloud top or SST. When clear-sky pixels are not involved (Fig. 9c), the $TB_{10.8}$ in the western Pacific Ocean and most parts of the Indian Ocean is lower than 280 K and that in the northeastern and southeastern Pacific Ocean can be as high as 284 K. When there are clear-sky pixels involved (Fig. 9d), the $TB_{10.8}$ in Pacific ITCZ areas is around 282–284 K and those in the south and north of the Pacific ITCZ are all beyond 284 K (some parts are even beyond 286 K). In Indian Ocean areas, the range is approximately 282–286 K. When the two situations are compared, the $TB_{10.8}$ of warm rain with clear sky is higher than that of warm rain without clear sky, by 5 K, and the number can even be 8 K in the monsoon region. As shown in Fig. 8, partial filling arises more easily in the monsoon region. Sometimes, two or more clear-sky pixels may be contained in a single warm-rain pixel because clear-sky pixels are more likely to occur in the monsoon warm precipitation. So, $TB_{10.8}$ in this area will be apparently enhanced when the average value is calculated.

The 17-dBZ echo-top height of warm-rain pixels in two situations is shown in Figs. 9e and 9f, in which the developmental height of the precipitation cloud is exhibited. When there are no clear-sky pixels involved (Fig. 9e), the average echo-top height of warm rain in the monsoon regions, such as the northwestern Pacific Ocean and north of the Indian Ocean, is higher than

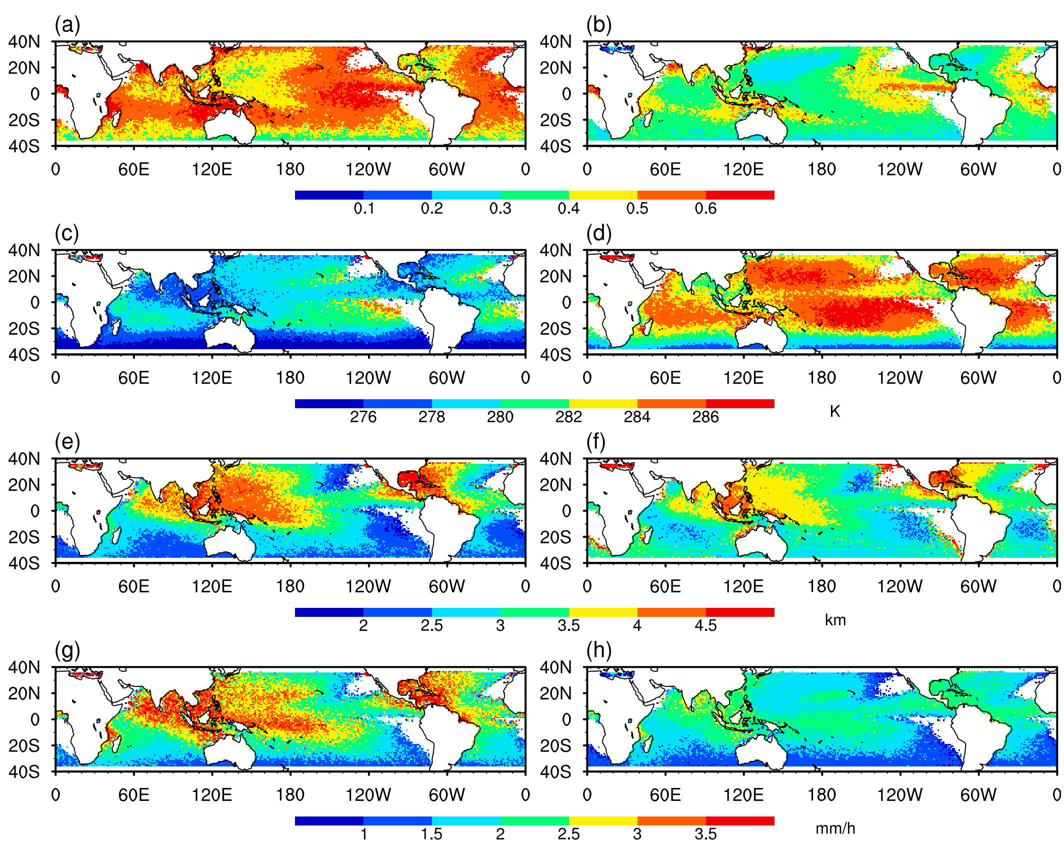

FIG. 9. (a),(b) Average $RF_{0.63}$, (c),(d) average $TB_{10.8}$, (e),(f) 17-dBZ echo-top height, and (g),(h) rain rate of warm-rain pixels at 0800–1600 LT: pixels (left) without and (right) with clear sky.

3.5 km on average, and the maximum could be 4.5 km, whereas that in the northeastern and southeastern Pacific Ocean, as well as the southern Indian Ocean, is apparently lower at just 2–3 km. In the northwestern Pacific Ocean and northern Indian Ocean, the echo-top height of pixels with clear sky is smaller than that of pixels without clear sky, by about 0.5 km. Yet in the northeastern and southeastern Pacific Ocean, where there are areas with pervasively warm cloud (Short and Nakamura 2000; Liu and Zipser 2009), the difference between the situations with and without clear-sky pixels is not large. In areas near the west coasts of continents, the situation with clear sky is mildly higher, by about 0.5 km. As mentioned during the sample-based results, some "fake" warm rain with an extremely low cloud-top temperature can also be involved in warm rain without clear-sky pixels. That is, thick and cold mixed cloud is mingled among several warm-cloud pixels with higher cloud-top temperature; however, the weighted average $TB_{10.8}$ is still higher than 273 K. For such warm-rain pixels, precipitation of the coldest spectral pixel is captured by PR, making its echo-top height the highest. This structure of precipitation cloud is usually seen in monsoon areas like the northwestern Pacific Ocean and northern Indian Ocean. Warm-rain pixels with clear sky are usually isolated or at the edges of rain cases, whereas those without clear sky generally occupy a large part of warm-cloud cases. The entire rain-top height of warm-rain cases in the southeastern and northeastern Pacific Ocean changes mildly. However, in isolated precipitation pixels it is hard to judge whether they might develop to vigorous precipitation, so the echo-top height of warm-rain pixels with clear sky may be counted as higher.

The rain rate of warm rain under two situations is shown in Figs. 9g and 9h. When clear-sky pixels are not involved (Fig. 9g), the rain rate of the warm tongue area and both monsoon regions (northern Indian Ocean and northwestern Pacific Ocean) is very high, mostly greater than 3 mm h^{-1}. There is a higher rain rate in Indonesian sea areas (sometimes higher than 3.5 mm h^{-1}), and the rain rate in the southeastern Pacific Ocean does not reach 2.5 mm h^{-1}. The rain rate of warm rain with clear-sky pixels involved is lower than that without clear sky by 1.5 mm h^{-1}. In the southeastern Pacific Ocean and the southern Indian Ocean, the rain rate of warm rain with clear sky is also lower, and there is a difference between them of about 0.5 mm h^{-1}. As can be analyzed from the examples shown in Fig. 8, convection is active in the monsoon regions, and sometimes several subscale convective cases also exist. A fraction of the central pixels' $TB_{10.8}$ in the PR resolution is even lower than 273 K. Most pixels without clear sky in the monsoon regions are this kind of convective central pixel, and so there is a very high rain rate. However, pixels with clear sky are mostly located at the rain-case edge in the monsoon regions, and there is an apparent difference in the rain rate between these two kinds of pixels. In other regions, precipitation is mainly stratiform, so there is only a small difference between central pixels and edge pixels.

4. Discussion and conclusions

In the introduction of this paper, the methods that use satellite-based instruments to detect warm rain were reviewed. Specifically, precipitation pixels are mainly taken as base points directly, with VIR–IR pixels nearest to them chosen or all VIR–I IR pixels in its resolution directly used to calculate the weighted average to confirm the spectral information in rain pixels, and then the cloud-top temperature is available to judge the presence of warm cloud. However, the effects when data of different resolution are merged to study warm rain remain unknown. In this study, a new 15-yr dataset was established, in which all VIRS information in the PR resolution was included. Marine warm-rain pixels in the tropics and subtropics (40°N–40°S) in summer (June–August) were recognized by using this dataset, along with the general method of using the weighted average $TB_{10.8}$ to recognize warm cloud. Their physical parameters and intrinsic spectral characteristics were then studied to try to reveal the physical parameters and spectral characteristics under different VIRS pixel-filling situations.

The results showed that not all $TB_{10.8}$ values were higher than 273 K in warm-rain pixels, as determined by using the weighted average $TB_{10.8}$, and in some areas were even lower than 265 K. Yet, there was actually no cloud involved in some areas of warm-rain pixels. Statistics show that the amount of clear-sky pixels, within warm-rain pixels, is 5 times as many as cold pixels. On the basis of this situation, warm-rain pixels were divided into warm-rain pixels with and without clear sky. Generally, clear-sky pixels are corresponding to high TB_{av} and low RF_{av}. Using statistical analysis, the physical parameters and spectral characteristics of the two kinds of warm rain were found to differ from one another. When the weighted average $TB_{10.8}$ was constant, the difference in brightness temperature tended to be higher in warm-rain pixels with clear sky. The distribution of $TB_{10.8}$ during daytime and at nighttime differed mildly. When the weighted average $TB_{10.8}$ and the difference in brightness temperature were constant simultaneously, the echo-top height of warm-rain pixels with clear sky tended to be higher, and the rain rate tended to be lower.

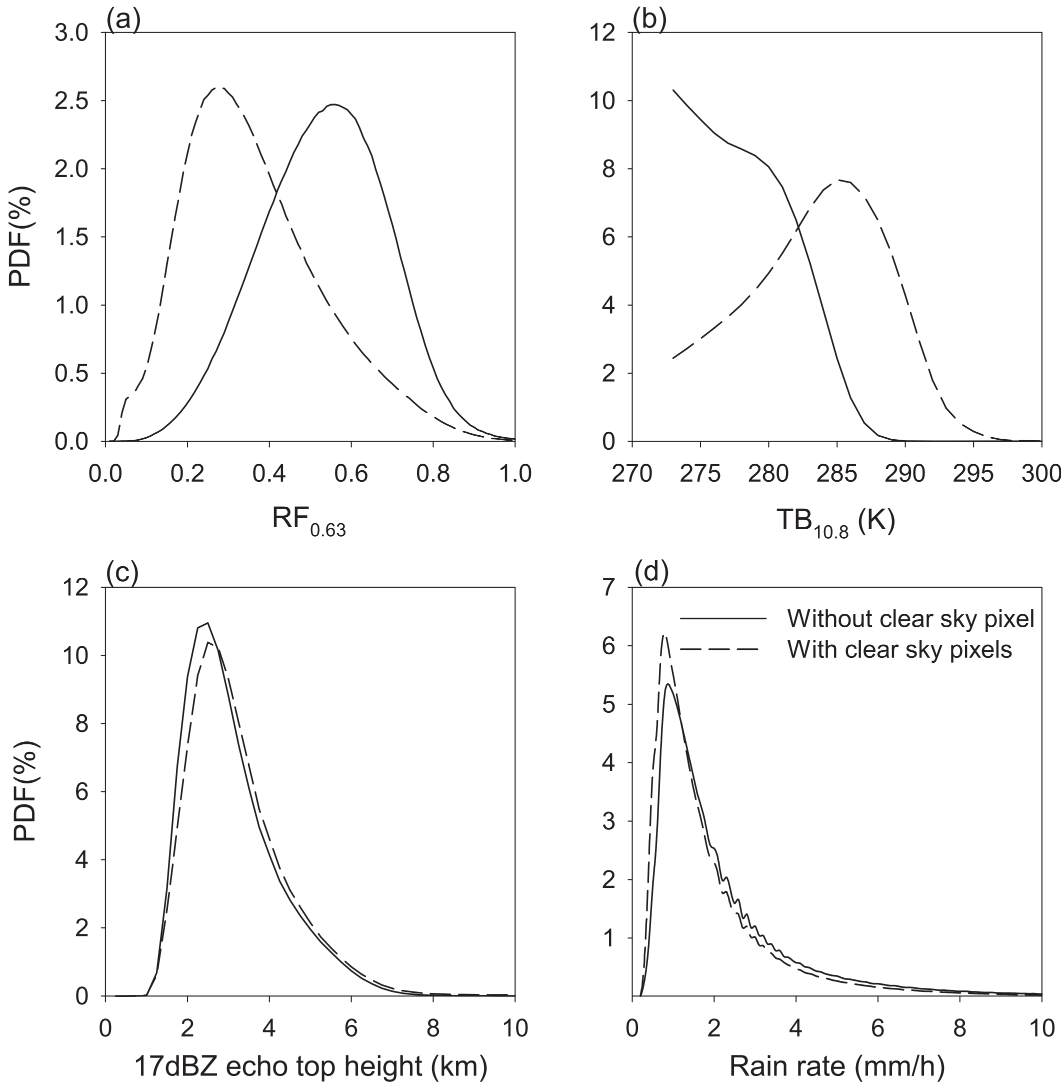

FIG. 10. PDFs of parameters in warm-rain pixels at 0800–1600 LT over 1998–2012. Solid and dashed lines stand for pixels without and with clear sky, respectively.

Clear sky was not involved in over 50% of warm-rain pixels in the Southern Hemisphere, whereas there was less than 30% in the Northern Hemisphere during daytime (0800–1600 LT). The $RF_{0.63}$ of warm-rain pixels without clear sky was around 0.1–0.2 greater than the $RF_{0.63}$ of that with clear sky during daytime, the $TB_{10.8}$ was 5–8 K lower than pixels with clear sky, the rain rate was 0.5–1.5 mm h^{-1} higher, and the difference in echo-top height mainly depended on the region. In monsoon areas, such as the northwestern Pacific Ocean and northern Indian Ocean, the physical parameters and spectral characteristics of warm-rain pixels were influenced most by whether or not clear-sky pixels were involved.

When discussing whether pixels with clear sky influence certain parameters, the distributions and differences of those parameters should be first considered. Figure 10 shows the systematic difference and distribution of various parameters in the two kinds of pixels. It is worth noting that both show one peak for $RF_{0.63}$. $TB_{10.8}$ peaks at 286 K with clear sky. However, when pixels are without clear sky, the proportion decreases as $TB_{10.8}$ increases. When $TB_{10.8}$ is greater than 280 K, its proportion decreases rapidly and moves closer to 0, after 288 K. The echo-top height of warm-rain pixels without clear sky is 0.25 km lower than that with clear sky during daytime, and the rain rate is higher and more widely distributed. In summary, the overall difference between the two kinds of pixels in terms of distribution is obvious, especially for the spectral characteristics provided by VIRS, which may have a serious impact on retrieving cloud parameters.

So, what scientific problems can be solved by using the difference obtained through the dataset? First, at the subscale of PR pixels, the partial-filling effect exists; thus, when studying slight precipitation or small rain cases that consist of a few PR pixels, the errors caused by partial filling should be considered. When planning large-scale or long-term research, these kinds of small rain cases can even be expelled. Liu et al. (2008) and Liu and Zipser (2009) defined precipitation events as containing at least four PR pixels. However, four-pixel precipitation events still seem too small, in that $TB_{10.8}$ changes severely (around 161.9°E in Fig. 2d). Second, because of a low height of the warm-rain top and a high temperature at the top of warm rain, the situation whereby edges of PR pixels are clear sky should be considered more fully when warm rain is studied. When warm rain is identified using weighted average brightness temperature of VIRS in the PR resolution or through the brightness temperature in the nearest pixel, clear-sky parts should be expelled first or it may cause problems in retrieving cloud parameters. It is possible that more warm-rain pixels over oceans are attached to cold precipitation systems than Liu and Zipser (2009) described because some areas in warm-rain pixels are even lower than 265 K. Besides, parts of rain pixels are identified as warm cloud, but sometimes mixed-cloud pixels may be intermingled and the gradient of $TB_{10.8}$ is large, meaning the existence of rising and sinking motion and an unstable atmospheric structure. Although TRMM can only detect instantaneous processes and cannot judge developmental processes of precipitation, it can be judged that warm rain with mixed-cloud pixel and a large $TB_{10.8}$ gradient in PR pixels may be unstable and most probably a "temporary" warm-rain event. At any time it can develop into deep precipitation.

There are several uncertainties associated with the clear-sky threshold and partial-filling effect in the subscale of VIRS pixels. Although 3 K is a reasonable threshold for clear sky, uncertainties in some parameters, such as SST and satellite observation, can cause bias of cloud detection. Quantitatively, every 1-K increase in the threshold from 0 to 6 K increases the number of warm-rain pixels, which contain clear-sky pixels, by 3%–9%. Additionally, the partial-filling effect can also exist in VIRS pixels, which may cause more error than what is estimated in this paper. Future use of the high-resolution VIR–IR and precipitation observation will mitigate the beam-filling problem, and future work will propose an effective method for identifying warm rain using satellite observation.

Acknowledgments. Thanks are given to three anonymous reviewers for valuable suggestions. This work is supported by the National Natural Science Foundation of China (NSFC Grants 91337213, 41230419, and 41675041), the Third Tibetan Plateau Scientific Experiment: Observations for Boundary Layer and Troposphere (Grant GYHY201406001), and the Special Funds for Public Welfare of China (Grant GYHY201306077). Thanks also are extended to Goddard Space Flight Center for providing PR 2A25 data.

REFERENCES

Awaka, J., T. Iguchi, H. Kumagai, and K. Okamoto, 1997: Rain type classification algorithm for TRMM Precipitation Radar. *Proc. 1997 Int. Geoscience and Remote Sensing—A Scientific Vision for Sustainable Development IGARSS '97*, Singapore, IEEE, 1633–1635, doi:10.1109/IGARSS.1997.608993.

Beard, K. V., and H. T. Ochs, 1993: Warm-rain initiation: An overview of microphysical mechanisms. *J. Appl. Meteor.*, **32**, 608–625, doi:10.1175/1520-0450(1993)032<0608:WRIAOO>2.0.CO;2.

Chen, R. Y., Z. Li, R. J. Kuligowski, R. Ferraro, and F. Weng, 2011: A study of warm rain detection using A-Train satellite data. *Geophys. Res. Lett.*, **38**, L04804, doi:10.1029/2010GL046217.

Chiu, J. C., and G. W. Petty, 2006: Bayesian retrieval of complete posterior PDFs of oceanic rain rate from microwave observations. *J. Appl. Meteor. Climatol.*, **45**, 1073–1095, doi:10.1175/JAM2392.1.

Cox, S. K., D. McDougal, D. Randall, and R. Schiffer, 1987: FIRE—The First ISCCP Regional Experiment. *Bull. Amer. Meteor. Soc.*, **68**, 114–118, doi:10.1175/1520-0477(1987)068<0114:FFIRE>2.0.CO;2.

Fu, Y. F., D. Liu, Y. Wang, R. Yu, Y. Xu, and R. Cheng, 2007: Characteristics of precipitating and non-precipitating clouds in Typhoon Ranan as viewed by TRMM combined measurements (in Chinese). *Acta Meteor. Sin.*, **65**, 316–328.

Gabella, M., E. Morin, and R. Notarpietro, 2011: Using TRMM spaceborne radar as a reference for compensating ground-based radar range degradation: Methodology verification based on rain gauges in Israel. *J. Geophys. Res.*, **116**, D02114, doi:10.1029/2010JD014496.

Guan, L., H. Kawamura, and H. Murakami, 2003: Retrieval of sea surface temperature from TRMM VIRS. *J. Oceanogr.*, **59**, 245–249, doi:10.1023/A:1025551507476.

Holland, J. Z., and E. M. Rasmusso, 1973: Measurements of atmospheric mass, energy, and momentum budgets over a 500-kilometer square of tropical ocean. *Mon. Wea. Rev.*, **101**, 44–55, doi:10.1175/1520-0493(1973)101<0044:MOTAME>2.3.CO;2.

Kirstetter, P. E., Y. Hong, J. J. Gourley, M. Schwaller, W. Petersen, and Q. Cao, 2015: Impact of sub-pixel rainfall variability on spaceborne precipitation estimation: Evaluating the TRMM 2A25 product. *Quart. J. Roy. Meteor. Soc.*, **141**, 953–966, doi:10.1002/qj.2416.

Kubar, T. L., D. L. Hartmann, and R. Wood, 2009: Understanding the importance of microphysics and macrophysics for warm rain in marine low clouds. Part I: Satellite observations. *J. Atmos. Sci.*, **66**, 2953–2972, doi:10.1175/2009JAS3071.1.

Kummerow, C., W. Barnes, T. Kozu, J. Shiue, and J. Simpson, 1998: The Tropical Rainfall Measuring Mission (TRMM) sensor package. *J. Atmos. Oceanic Technol.*, **15**, 809–817, doi:10.1175/1520-0426(1998)015<0809:TTRMMT>2.0.CO;2.

Lau, K. M., and H. T. Wu, 2003: Warm rain processes over tropical oceans and climate implications. *Geophys. Res. Lett.*, **30**, 2290, doi:10.1029/2003GL018567.

Lavoie, R. L., 1967: Warm rain project in Hawaii. *Tellus*, **19**, 347, doi:10.1111/j.2153-3490.1967.tb01488.x.

Lebsock, M. D., and T. S. L'Ecuyer, 2011: The retrieval of warm rain from CloudSat. *J. Geophys. Res.*, **116**, D20209, doi:10.1029/2011JD016076.

Liu, C., and E. J. Zipser, 2009: "Warm rain" in the tropics: Seasonal and regional distributions based on 9 yr of TRMM data. *J. Climate*, **22**, 767–779, doi:10.1175/2008JCLI2641.1.

——, and ——, 2014: Differences between the surface precipitation estimates from the TRMM Precipitation Radar and passive microwave radiometer version 7 products. *J. Hydrometeor.*, **15**, 2157–2175, doi:10.1175/JHM-D-14-0051.1.

——, ——, D. Cecil, S. Nesbitt, and S. Sherwood, 2008: A cloud and precipitation feature database from nine years of TRMM observations. *J. Appl. Meteor. Climatol.*, **47**, 2712–2728, doi:10.1175/2008JAMC1890.1.

Liu, G., J. A. Curry, and R.-S. Sheu, 1995: Classification of clouds over the western equatorial Pacific Ocean using combined infrared and microwave satellite data. *J. Geophys. Res.*, **100**, 13 811–13 826, doi:10.1029/95JD00823.

Liu, Q., and Y. F. Fu, 2010: Comparison of radiative signals between precipitating and non-precipitating clouds in frontal and typhoon domains over East Asia. *Atmos. Res.*, **96**, 436–446, doi:10.1016/j.atmosres.2010.02.003.

Liu, X. T., Q. Liu, Y. F. Fu, and R. Li, 2014: Daytime precipitation identification scheme based on multiple cloud parameters retrieved from visible and infrared measurements. *Sci. China Earth Sci.*, **57**, 2112–2124, doi:10.1007/s11430-014-4870-z.

Min, Q., R. Li, X. Wu, and Y. Fu, 2013: Retrieving latent heating vertical structure from cloud and precipitation profiles—Part I: Warm rain processes. *J. Quant. Spectrosc. Radiat. Transfer*, **122**, 31–46, doi:10.1016/j.jqsrt.2012.11.030.

Schumacher, C., and R. A. Houze, 2003: The TRMM Precipitation Radar's view of shallow, isolated rain. *J. Appl. Meteor.*, **42**, 1519–1524, doi:10.1175/1520-0450(2003)042<1519:TTPRVO>2.0.CO;2.

Short, D. A., and K. Nakamura, 2000: TRMM radar observations of shallow precipitation over the tropical oceans. *J. Climate*, **13**, 4107–4124, doi:10.1175/1520-0442(2000)013<4107:TROOSP>2.0.CO;2.

Steiner, M., R. Houze, and S. Yuter, 1995: Climatological characterization of three-dimensional storm structure from operational radar and rain gauge data. *J. Appl. Meteor.*, **34**, 1978–2007, doi:10.1175/1520-0450(1995)034<1978:CCOTDS>2.0.CO;2.

Waymire, E., V. K. Gupta, and I. Rodriguez-Iturbe, 1984: A special theory of rainfall intensity at the meso-β scale. *Water Resour. Res.*, **20**, 1453–1465, doi:10.1029/WR020i010p01453.

Wilheit, T. T., and C. D. Kummerow, 2009: Use of the TRMM-PR for estimating the TMI beam filling correction. *J. Meteor. Soc. Japan*, **87A**, 255–263, doi:10.2151/jmsj.87A.255.

Yang, Y.-J., D.-R. Lu, Y.-F. Fu, F.-J. Chen, and Y. Wang, 2015: Spectral characteristics of tropical anvils obtained by combining TRMM Precipitation Radar with visible and infrared scanner data. *Pure Appl. Geophys.*, **172**, 1717–1733, doi:10.1007/s00024-014-0965-x.